JGR Space Physics

RESEARCH ARTICLE
10.1029/2023JA032250

Modeling the Global Distribution of Chorus Wave Induced Relativistic Microburst Spatial Characteristics

Ning Kang[1], Jacob Bortnik[1], Qianli Ma[1], and Seth Claudepierre[1]

[1]Department of Atmospheric and Oceanic Sciences, University of California, Los Angeles, CA, USA

Key Points:

- Based on statistical chorus and electron distributions, the global distribution of relativistic microburst scale size is modeled
- Dawn and night sectors are fairly similar in precipitation scale size, and dayside has larger maximum precipitation flux and smaller width
- The keV electron populations on dayside play a critical role on the MeV electron precipitation intensity and the microburst scale size

Correspondence to:

N. Kang,
nkang20@atmos.ucla.edu

Citation:

Kang, N., Bortnik, J., Ma, Q., & Claudepierre, S. (2024). Modeling the global distribution of chorus wave induced relativistic microburst spatial characteristics. *Journal of Geophysical Research: Space Physics*, *129*, e2023JA032250. https://doi.org/10.1029/2023JA032250

Received 2 NOV 2023
Accepted 25 FEB 2024

Author Contributions:

Conceptualization: Jacob Bortnik
Data curation: Qianli Ma
Formal analysis: Ning Kang, Jacob Bortnik
Funding acquisition: Jacob Bortnik, Seth Claudepierre
Investigation: Ning Kang, Jacob Bortnik, Qianli Ma, Seth Claudepierre
Methodology: Ning Kang, Jacob Bortnik
Project administration: Jacob Bortnik
Software: Ning Kang, Jacob Bortnik
Supervision: Jacob Bortnik
Validation: Ning Kang, Jacob Bortnik
Visualization: Ning Kang, Jacob Bortnik
Writing – original draft: Ning Kang
Writing – review & editing: Ning Kang, Jacob Bortnik, Qianli Ma, Seth Claudepierre

Abstract The full spatiotemporal distribution of chorus wave-induced relativistic electron microburst is modeled for chorus waves originated from different L shells and MLTs, based on the newly developed numerical precipitation model (Kang et al., 2022, https://doi.org/10.1029/2022gl100841). The wave-particle interaction process that induces each microburst is analyzed in detail, and its relation to the chorus wave propagation effects is explained. The global distribution of maximum precipitation fluxes and scale sizes of relativistic microbursts is then obtained by modeling chorus waves at different L-shells and local times. The characteristics of dawn and midnight sector microbursts have little difference, but the noon sector has much larger maximum flux and much smaller full width at half maximum, which may be due to dayside's low electron flux in the Landau resonance range. This suggests the controlling effect of keV electrons on the MeV electron precipitation intensity and properties and the overall relativistic electron loss in the outer radiation belt.

1. Introduction

Microbursts are impulsive, energetic electron precipitation bursts whose typical duration is <1s. They were first discovered through balloon arrays (Anderson & Milton, 1964), and have been extensively observed and studied through low earth orbit (LEO) spacecrafts (Douma et al., 2017; Imhof et al., 1992; Lorentzen, Blake, et al., 2001; Lorentzen, Looper, & Blake, 2001; O'Brien et al., 2003; Zhang et al., 2022). Microbursts are believed to be important for the Earth's radiation belt dynamics, especially as one of the major loss mechanisms of relativistic electrons in the heart of the outer radiation belt (Douma et al., 2019; Lorentzen, Blake, et al., 2001; O'Brien et al., 2003; Thorne et al., 2005).

It is widely accepted that chorus waves are a major driver of relativistic microbursts. Previous statistical works (Douma et al., 2017; Nakamura et al., 2000; Zhang et al., 2022) show that microbursts have very similar statistical properties as chorus waves (Li et al., 2009), including higher occurrence rates during more disturbed times, similar high-occurrence at the same L shell and MLT ranges, and predominantly occurring outside the plasmapause. Conjunctions between equatorial chorus waves and low-altitude microbursts have also been reported (Breneman et al., 2017; Kersten et al., 2011; Lorentzen, Looper, & Blake, 2001). However, the detailed mechanism of chorus waves driving relativistic microburst and the qualitative contribution of precipitation flux through chorus-driven relativistic microbursts are still not fully understood. Also, the scale size of microbursts, as an important element in quantifying electron loss, has very limited observational evidences and modeling predictions, and is poorly understood about its connection to their chorus wave drivers.

Many previous modeling works (Chen et al., 2020, 2021; Hikishima et al., 2010; Miyoshi et al., 2010, 2020; Ozaki et al., 2021, 2022; Saito et al., 2012) on microbursts have been dedicated to addressing these questions. However, most of the modeling works are constrained to a group of parallel-propagating chorus waves on a single field line or a narrow L shell range around the source region, which is not realistic in the absence of a duct and will not fully reflect the propagation effects of chorus waves in the more common unducted case. Recently, Kang et al. (2022) developed a model that includes the full propagation effects of chorus waves, and addressed its importance on microburst. This model is also able to simulate the full spatiotemporal distribution of the precipitation flux induced by chorus waves, using which Kang et al. (2022) conducted an event-based simulation and predicted a relativistic microburst scale size of several tens km, which agrees with previous observation works (Blake et al., 1996; Crew et al., 2016; Parks, 1967; Shumko et al., 2018, 2020). Compared to previous models of chorus-driven electron precipitation (e.g., Bortnik & Thorne, 2007, Figure 3) that assumed a chorus source region distributed in space, and initial wave normal angles set at the Gendrin angle (which was believed to be the most representative chorus model at the time), the model of Kang et al. (2022) assumed a spatial chorus point source, and a wide distribution of WNAs, which is more representative of the present understanding of the chorus source characteristics.

In this work, we will apply the newly developed model of Kang et al. (2022) to conducting simulations under different wave and plasma conditions at different L shells and MLTs, thus attempting to construct a global distribution of the spatial characteristics of chorus wave induced relativistic microbursts. This model provides a theoretical comparison for recent statistical works on relativistic microburst (Shumko et al., 2021), and the global distribution of microburst scale size is also an important ingredient in better understanding the role that chorus wave induced relativistic microburst plays in the global energetic electron loss (Pailoor et al., 2023). We introduce our simulation code and the simulation setup based on the previous statistical chorus and electron distributions in Section 2, and in Section 3 we present our results in detail. In Section 4, we discuss the simulation results and summarize the key findings.

2. Model Description

2.1. Simulation Code

The precipitation simulation code used in this work is based on the framework of the Whistler Induced Particle Precipitation (WIPP) code (Bortnik et al., 2006a, 2006b; Kang, 2023; Kang & Bortnik, 2022), which was originally designed for the precipitation modeling of lightning induced whistlers. We updated it to accommodate a chorus wave-induced precipitation scenario. The workflow of the model is: (a) first conduct an extensive chorus wave ray tracing simulation, then (b) construct the wave characteristics on each field line based on the ray trajectories crossing that field line, and finally (c) implement the wave characteristics on single field lines to conduct a pitch angle (PA) scattering calculation, which further provides (d) the energy-time (E-t) spectrum of the precipitation flux at the ionospheric footpoint of each field line. Here we briefly describe the workflow of the code.

In the ray tracing stage (i), we use the Stanford VLF Ray Tracer (Inan & Bell, 1977). We initialize rays at an equatorial chorus wave source point (and extend to a finite sized source region using the method described later) with 151 frequencies ranging from $0.1f_{ce}$ to $0.5f_{ce}$ (f_{ce} is the local electron gyrofrequency at the equatorial source region) and 51 initial WNAs ranging from -60° to 60° (positive/negative WNA means that the wave vector is oriented outward/Earthward), which makes up 7,701 rays to be traced in total. All rays are damped through Landau damping, which is calculated based on the method of Brinca (1972). This method requires a hot electron velocity distribution, which can be inferred using the method of Bortnik et al. (2007) if an electron flux energy spectrum is given. We then use the ray path interpolation method introduced by Bortnik et al. (2003) to generate ~311 million ray paths based on the 7,701 "sampled" rays that were actually traced by the ray tracer, thus reducing the discreteness of the ray path ensemble and smoothing the wave characteristic profiles generated in the next step.

In order to generate the wave characteristics on a single field line, the field line is divided into multiple small segments, and each small segment undergoes a check-crossing procedure with the 311 million rays to locate the rays that contribute to this segment and record their characteristics (e.g., the crossing time, frequency, amplitude and dispersion parameters), thus obtaining the desired spatiotemporal profile of the chorus wave at multiple points along a given field line. With these wave characteristics, the PA scattering due to different resonance modes (see Section 3.2 and Equation 5) can be calculated under a quasi-linear framework for a trapped electron (with energy E) traveling on this field line from the equator. Combined with a trapped flux model the scattered PA can be converted to the desired precipitation flux E-t spectrum through a convolutional operation. This part of our code is identical to the original WIPP code and readers who are interested can find more technical details in Bortnik et al. (2006a).

To take the finite size of chorus wave source region into consideration, we use the fact that the size of chorus wave source region is usually only several hundred km or $<0.1R_E$ (R_E = 6370 km is the Earth radius), which is much smaller than the L shell range covered by the ray paths (see the ray tracing results in Figure 2). We also assume that the ray paths of two rays are almost parallel to each other if their equatorial source points are close enough. In other words, if their equatorial source points are separated by $d \ll R_E$, then one of the ray paths can be well approximated by another which is displaced by d. This assumption is valid because we expect the ray paths in a smooth magnetosphere to be smooth and continuous. Therefore, if we have the precipitation flux on different field lines ($F_{ps}(L)$) that is calculated from a point source whose L shell is L_0, and the wave power density function ($g(L)$) over a small radial range of source region around L_0, we can directly calculate the precipitation flux distribution $F(L)$ considering the finite sized source region by:

$$F(L) = \int F_{ps}(l)\, g(L - (l - L_0))\, dl. \tag{1}$$

This simple convolution method can help us extend our results from the point source case to the finite size source region case. When we choose the power density function $g(L) = \delta(L\ 1 - L_0)$, Equation 1 will reduce to the point source case $F(L) = F_{ps}(L)$. In this work, we assume the wave power distribution at the equatorial source region is a Gaussian function peaked at L_0 with a width given by ΔL:

$$g(L) = \frac{1}{\Delta L\sqrt{2\pi}} e^{-\frac{(L-L_0)^2}{2\Delta L^2}}, \tag{2}$$

so Equation 1 becomes

$$F(L) = \frac{1}{\Delta L\sqrt{2\pi}} \int F_{ps}(L - l)\, e^{-\frac{l^2}{2\Delta L^2}} dl. \tag{3}$$

We adopt a chorus source size of ~500 km according to Agapitov et al. (2018), and use twice of the standard variation (ΔL) of the Gaussian distribution as the scale length, thus setting the value of $\Delta L = 250$ km.

2.2. Statistical-Result-Based Model Setup

To investigate the global distribution characteristics of the relativistic microburst spatial scale size, we separately run the simulation at 3 different MLTs (0, 6, and 12) and 3 different L shells (5, 5.5, and 6) giving 9 different locations. These 9 locations are marked in Figure 1c by black crosses, in which the contours are the statistical results of lower band chorus wave power density near the magnetic equator during disturbed times (Ma et al., 2020). From Figure 1c we see that the chosen L shells cover the most important L shells where lower band chorus waves occur. Meanwhile, the MLT values (0, 6, and 12) are chosen to represent the 3 sectors (midnight, dawn and noon) where lower band chorus waves typically occur. These 9 locations reveal the general L-MLT distribution of relativistic microburst characteristics and spatial scale sizes.

We use a modified diffusive equilibrium (DE) model for the cold electron density in ray tracing which is critical for guiding the ray trajectories, following Bortnik et al. (2011). Three DE models are adopted for the simulation of the meridional plane density distribution for the 3 MLT sectors. We adjust the parameters in the DE model so that the equatorial density profile fits the equatorial Carpenter and Anderson (CA) model (Carpenter & Anderson, 1992) for each MLT. Figure 1b shows the density models we use. The solid lines are the DE models for the 3 MLTs that are used in the ray tracing, and the dashed lines are the CA models for each MLT. We can see that our DE model fit agrees well with the CA model, especially so for $L > 5$ where the ray paths are traced in this study. We use a dipole magnetic field model in ray tracing.

Both the Landau damping calculation and the conversion of the scattered PA into a precipitation flux need an energetic electron flux spectrum. Here we use the statistical result based on the data from Ma et al. (2020) to find the electron energy spectrum for the three different MLTs, which is shown in Figure 1a. As done in Ma et al. (2020), the trapped electron flux data are selected only when the chorus waves are observed to obtain the statistical electron flux distribution. These flux spectra are used as the equatorial trapped fluxes in the precipitation flux calculation. Following Kang et al. (2022) and Bortnik et al. (2006a), the flux PA distribution is assumed to be empty inside the loss cone and isotropic outside as the first-order assumption. The flux spectra in the energy range of $1 < E < 100$ keV (which is the major Landau resonance range, as indicated in Figures 3 and 4) are converted into an electron velocity distribution using the method of Bortnik et al. (2007), which is further used for Landau damping calculation.

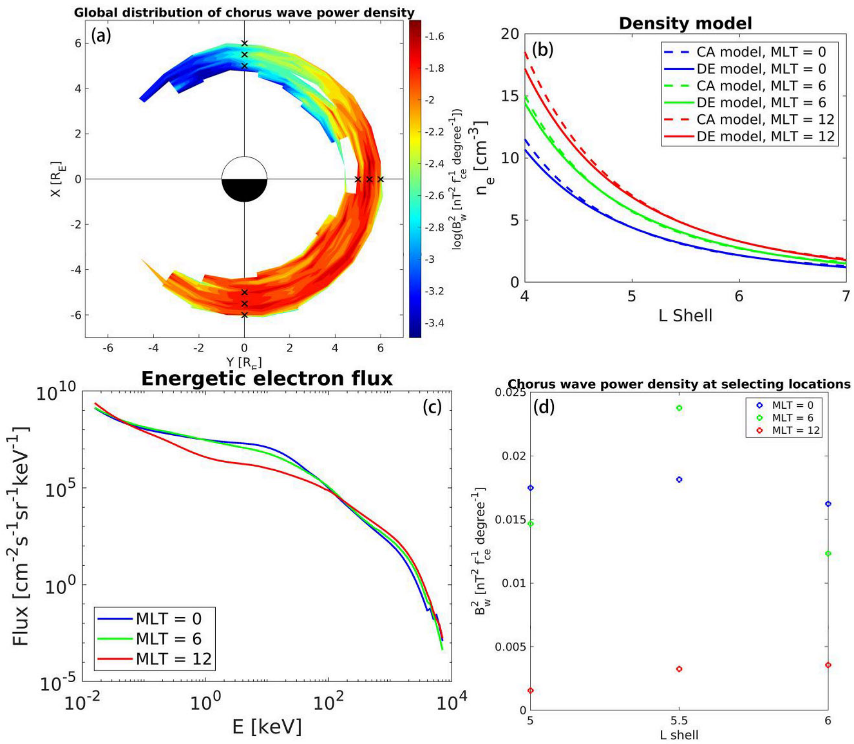

Figure 1. Data-driven model for plasma and waves, based on RBSP statistical results. The blue, green and red lines/circles are for MLT = 0, 6, and 12. (a) L-MLT distribution of chorus wave power density. The black crosses are the modeled chorus wave source points. (b) Equatorial density model. The dashed lines are the Carpenter-Anderson model, and the solid lines are the diffusive equilibrium model. (c) Electron flux energy spectrum for MLT = 0, 6, and 12. (d) The chorus wave power density of the modeled source points.

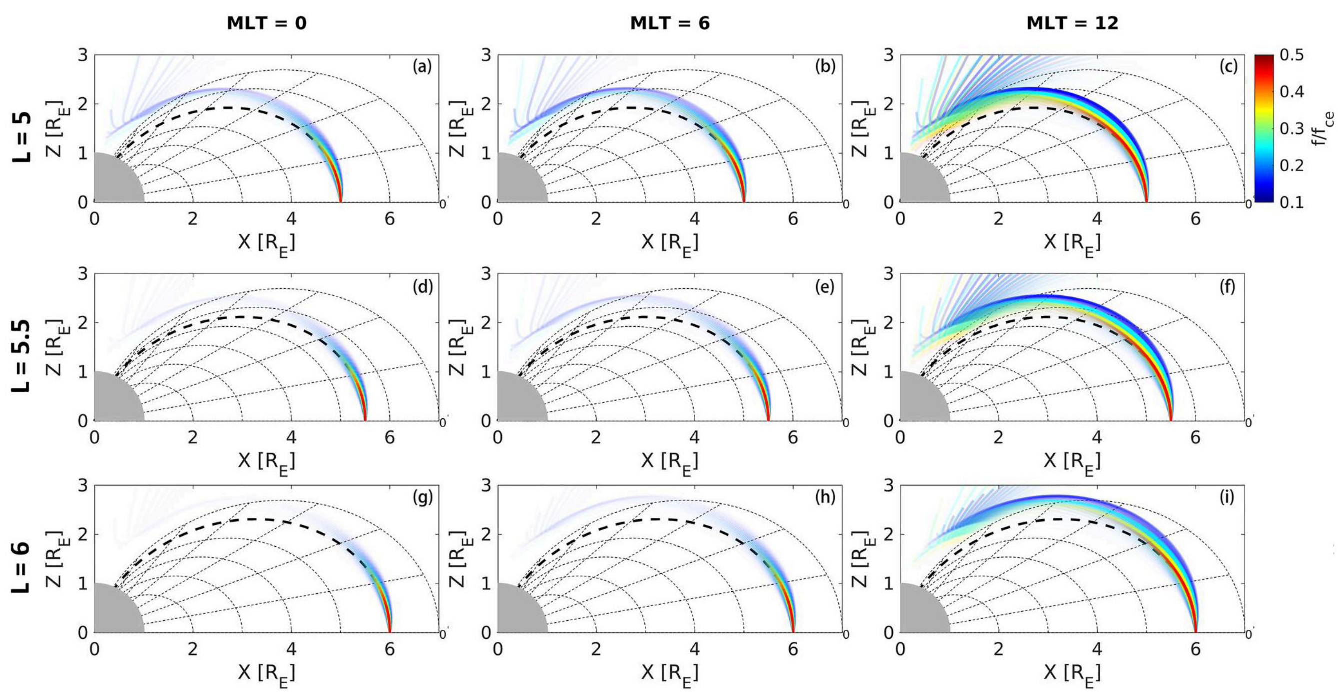

Figure 2. Ray paths of different frequencies for all modeled runs. Different frequencies are marked by different colors as shown by the color bar in the top right corner. The three rows are for $L = 5$, 5.5, and 6, and the three columns are for MLT = 0, 6, and 12, as indicated by the top and leftmost labels. The transparency of the rays indicates the ray power.

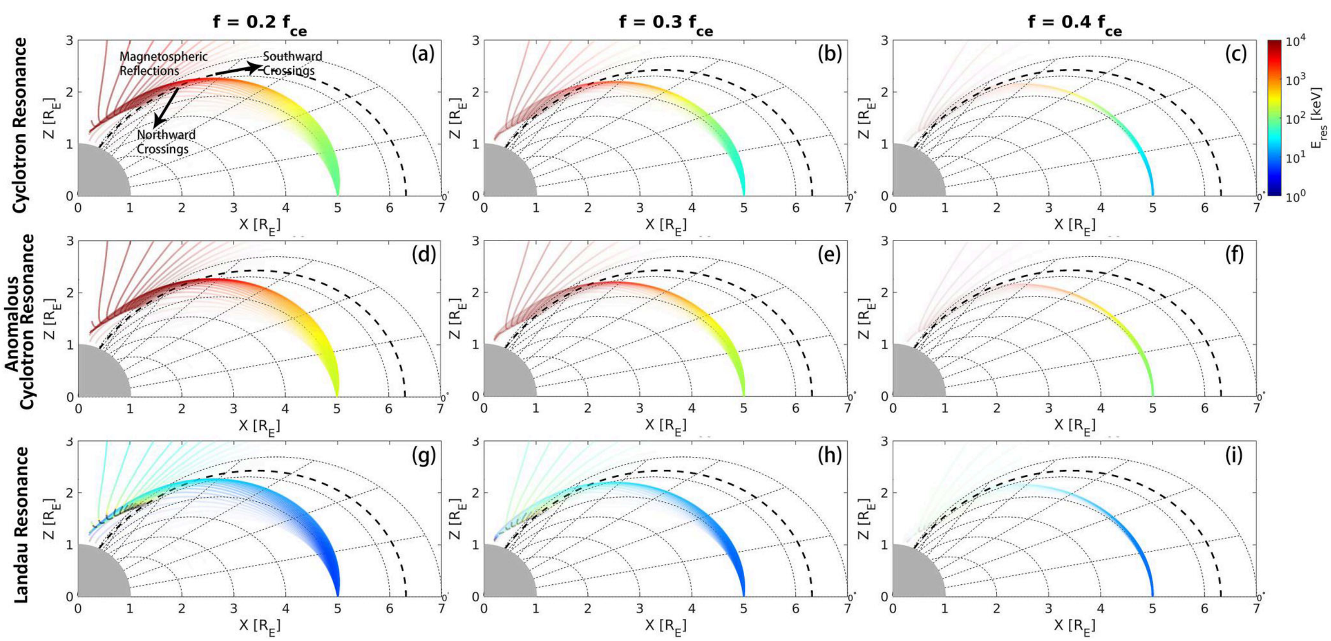

Figure 3. Resonance energy along ray paths for Run $L = 5$, MLT = 0. The three columns are rays with frequency 0.2, 0.3, and 0.4 source point gyrofrequency f_{ce}, and the three rows are for resonance energy through different resonance types (cyclotron, anomalous cyclotron and Landau resonance). The resonance energy is color coded as indicated by the color bar in the top right corner. The transparency of the rays indicates the ray power. The thick black dashed line indicates the field line of $L = 6.312$, whose precipitation flux E-t spectrum is shown in Figure 4.

We assume the initial chorus wave power at each source point follows a sine-shaped frequency distribution between $0.1 \sim 0.5 f_{ce}$, and a Gaussian WNA distribution. Specifically, the initial wave power density.

$$P(f,\theta) = \frac{0.1587 B_{w0}^2}{f_{ce}\Delta\theta}\sin\left(\frac{f-0.1f_{ce}}{0.4f_{ce}}\pi\right)e^{-\frac{\theta^2}{2\Delta\theta^2}}, \quad (4)$$

where f is the frequency and θ is the initial WNA. The initial WNA width $\Delta\theta$ is set to be 15°, and B_{w0}^2 is the average wave power (0.1587 is the normalized factor). The value of $\frac{0.1587 B_{w0}^2}{f_e\Delta\theta}$ is given from the lower band chorus wave amplitude statistical results in Figure 1c. The detailed ray power for each of the 9 runs are plotted in Figure 1d.

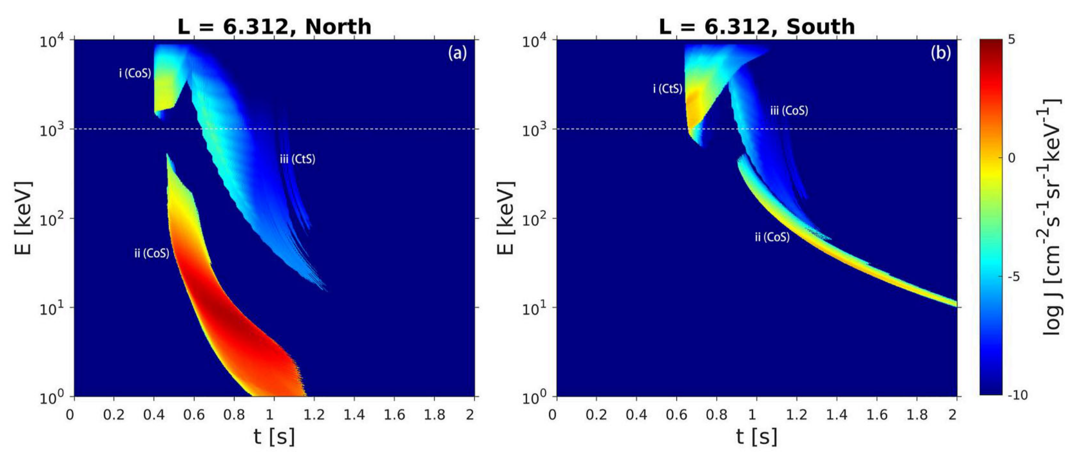

Figure 4. The precipitation flux E-t spectrum for field line $L = 6.312$ in Run $L = 5$, MLT = 0. Panels (a) and (b) precipitation on the Northern/Southern hemisphere foot points. The contour color is the precipitation flux. The white dashed lines marks the 1 MeV energy. Each panel has three parts marked by label i, ii, and iii. CoS and CtS means co-streaming and counter-streaming.

3. Results

3.1. Ray Tracing Results

Figure 2 shows the ray paths for 9 ray tracing simulation runs. Panels in different rows/columns represent ray paths for chorus wave source regions at different L shells and MLTs as labeled at the left/top of the figure. In each panel, rays of different frequencies are color coded according to the color bar on the top right, and for each frequency, 51 rays with different initial WNA are plotted. The transparency of the ray paths indicates the ray power.

Two important propagation properties are noted from the ray tracing results. First, for the non-ducted chorus waves, most of the wave power tends to propagate to slightly higher L shells. In all cases, for the latitude region $\lambda > 20^{\circ}$, there is no longer any significant wave power within the L shell of the chorus wave source region (the thick dashed line) since the rays have moved to higher L shells. This is in consistent with previous studies (Chen et al., 2020; Horne & Thorne, 2003; Miyoshi et al., 2015, 2020; Saito et al., 2012). Although the chorus wave power is usually considerably reduced at such high latitudes due to Landau damping, it is nevertheless the high latitude region instead of the low latitude region, that plays a critical role in generating relativistic electron microbursts, as will be illustrated in the next subsection. That means we would generally expect relativistic microbursts to be observed at a higher latitude by low-Earth orbit satellites than the invariant latitude of the chorus wave source region. Furthermore, the relativistic microbursts will keep moving poleward (as projected onto the ionosphere) because as chorus waves propagate to higher latitudes, the remaining wave power will keep propagating to higher L shells and map to higher invariant latitudes.

A second important wave property is that chorus waves experience much weaker Landau damping on the dayside (MLT = 12) compared to the nightside. Figures 2c, 2f, and 2i show that dayside chorus waves can preserve a much larger portion of their wave power to high latitudes compared to similar L-shell waves at MLT = 0 or 6. This is a direct result of the low electron fluxes responsible for Landau damping, at 1–100 skeV. From Figure 1a we see that the dayside (MLT = 12, red line) electron flux level between 1 and 100 keV is one or two orders of magnitudes lower than those at MLT = 0 or 6 (blue and green lines). We will show that this is the key energy range for Landau resonance between chorus waves and electrons. The low electron fluxes at Landau resonance energy on the dayside result in low Landau damping rates, which makes it possible for the dayside chorus waves to retain significant amounts of wave power at very high latitudes compared to the waves at midnight and dawn.

We would also like to point out the formation of magnetospherically reflected (MR) waves, particularly on the dayside. Those are the waves that encounter a reflection at very high latitudes due to reaching their lower hybrid resonance point (Kimura, 1966; Smith & Angerami, 1968) and thus reverse their propagation direction (in this case, switch from northward to southward propagating). These waves are usually highly damped (power is 3–4 orders of magnitude lower), and the remaining power keeps propagate to higher L shells which can result in an additional component of electron precipitation.

3.2. Resonance Energy of Chorus Waves and Precipitated E-t Spectrum

To understand where the relativistic electrons are scattered to produce relativistic microbursts, we calculate the resonance energy of chorus waves along their ray paths. The resonance condition is given by

$$\omega - k_{\parallel} v_{\parallel} = m \frac{\Omega_e}{\gamma}, \tag{5}$$

where ω and $k_{\parallel}$ are the angular frequency and parallel wave number, $v_{\parallel}$, Ω_e and γ are the parallel velocity, unsigned gyrofrequency and relativistic Lorentz factor of the resonant electron, and m is the order of resonance which takes the value of any integer. The value of m determines the characteristic of the resonance. For $m > 0$, the resonance is counter-streaming, and for $m \leq 0$, the resonance is co-streaming. The most important resonance types are those with smallest $|m|$, which are cyclotron resonance ($m = 1$), anomalous cyclotron resonance ($m = -1$) and Landau resonance ($m = 0$). The resonance energy E_{res} is determined by

$$E_{\text{res}} = (\gamma - 1) m_e c^2, \tag{6}$$

10.1029/2023JA032250

where m_e is the mass of electron and c is the speed of light. γ is determined from Equation 5 noticing that $\gamma = \frac{1}{\sqrt{1-\frac{v_{\parallel}^2}{c^2 \cos^2 \alpha}}}$, where α is the PA of the electron. Thus E_{res} can be expressed as a function of ω,$k_{\parallel}$, Ω_e,α and m.

We use the run with a chorus wave source region location of $L = 5$, MLT $= 0$ as an example, which is shown in Figure 3. We calculate the resonance energy for three frequency modes 0.2, 0.3, and 0.4 f_{ce} (the three columns in Figure 3) and each for the normal cyclotron resonance, anomalous cyclotron resonance and Landau resonance (shown in the three rows in Figure 3). The transparency of the ray paths represents the ray power, and the resonance energy is color coded according to the color bar on top right.

From Figure 3 we see that the relativistic electron microburst is only generated due to the cyclotron and anomalous cyclotron resonance. Landau resonance is almost unable to scatter electrons with energies >1 MeV into the loss cone. Furthermore, even for cyclotron and anomalous cyclotron resonances, scattering the MeV electrons is only possible after chorus waves propagate to latitudes higher than 25°. Near the equatorial source region, the chorus waves can only scatter electrons with energy up to several hundred keV. In other words, relativistic electron microbursts are produced at high latitudes through cyclotron or anomalous cyclotron resonance. Ray tracing results shows that such resonances almost always occur at a higher L shell relative to the causative chorus wave source region.

Figure 4 illustrates the structure of the E-t spectrum of the precipitation flux on a certain field line, calculated from all rays that cross this field line and contribute to electron scattering. We use the field line at $L = 6.312$ (the thick dashed line in each of the panels of Figure 3) as an example, whose precipitated E-t spectrum is plotted in Figure 4. Panels (a) and (b) show the precipitated E-t spectrum in the northern and southern hemisphere on this field line, respectively. The asymmetry across hemispheres arises from our model assumption that the chorus wave element propagates northward from equatorial source region, thus the northern and southern asymmetry will be formed as a result of different types of resonances depending on whether the electrons are counter-streaming (CtS) or co-streaming (CoS).

There are three parts of the precipitation signature that are evident in both panels (labeled i, ii and iii), in which part (i) exceed 1 MeV and corresponds to the relativistic electron microburst. From Figure 3 we see that part (i) should be due to either cyclotron resonance or anomalous cyclotron resonance. Considering that cyclotron resonance is a counter-streaming interaction and anomalous cyclotron resonance is co-streaming, and that chorus waves propagate northward, we can identify part (i) in the northern hemisphere as being caused by anomalous cyclotron resonance and the one in the southern hemisphere as being cause by cyclotron resonance. Comparing the precipitation flux amplitude of part (i) in both hemispheres, we see that the one in the southern hemisphere is stronger, which agrees with the fact that cyclotron resonance is more effective than anomalous resonance. Although the energy of efficient CoS precipitation in the southern hemisphere is only above 800 keV, the chorus waves at lower latitudes could scatter lower energy (down to ∼10 keV) electrons through efficient cyclotron resonance at lower L shells (Figure 3), which are not detected at $L = 6.312$.

Another strong precipitation part is part (ii) in the northern hemisphere at lower energies. Comparing the electron energy range with the resonance energy shown in Figure 3 and the co-streaming nature of northern hemisphere precipitation, we can identify this part of precipitation as being due to Landau resonance. The resonance energy of Landau resonance is always below 1 MeV (below 1 keV to at most 500 keV), so this part of precipitation is not the direct focus of this work but is important for driving the pulsating and diffuse aurora (Nishimura et al., 2010, 2011; Thorne et al., 2010) which will be studied in future works.

Note that although the chorus waves are launched toward the northern hemisphere near the equator, there are also southward propagating waves, that is, the highly damped MR waves (one example marked in Figure 3a). These MR waves allow resonance modes with reversed streaming nature for both hemispheres. For example, part (iii) in the northern hemisphere is due to counter-streaming cyclotron resonance with MR waves, and parts (ii) and (iii) in the southern hemisphere are due to co-streaming Landau and anomalous cyclotron resonance with these MR waves, respectively. These three parts of the precipitation signature are of lesser significance because MR waves are highly damped, which results in very low scattering rates. As shown in Figure 4, the fluxes of part (iii) are 4–5 orders of magnitudes lower than part (i), and part (ii) in southern hemisphere is also 4–5 orders of magnitudes lower than those in northern hemisphere.

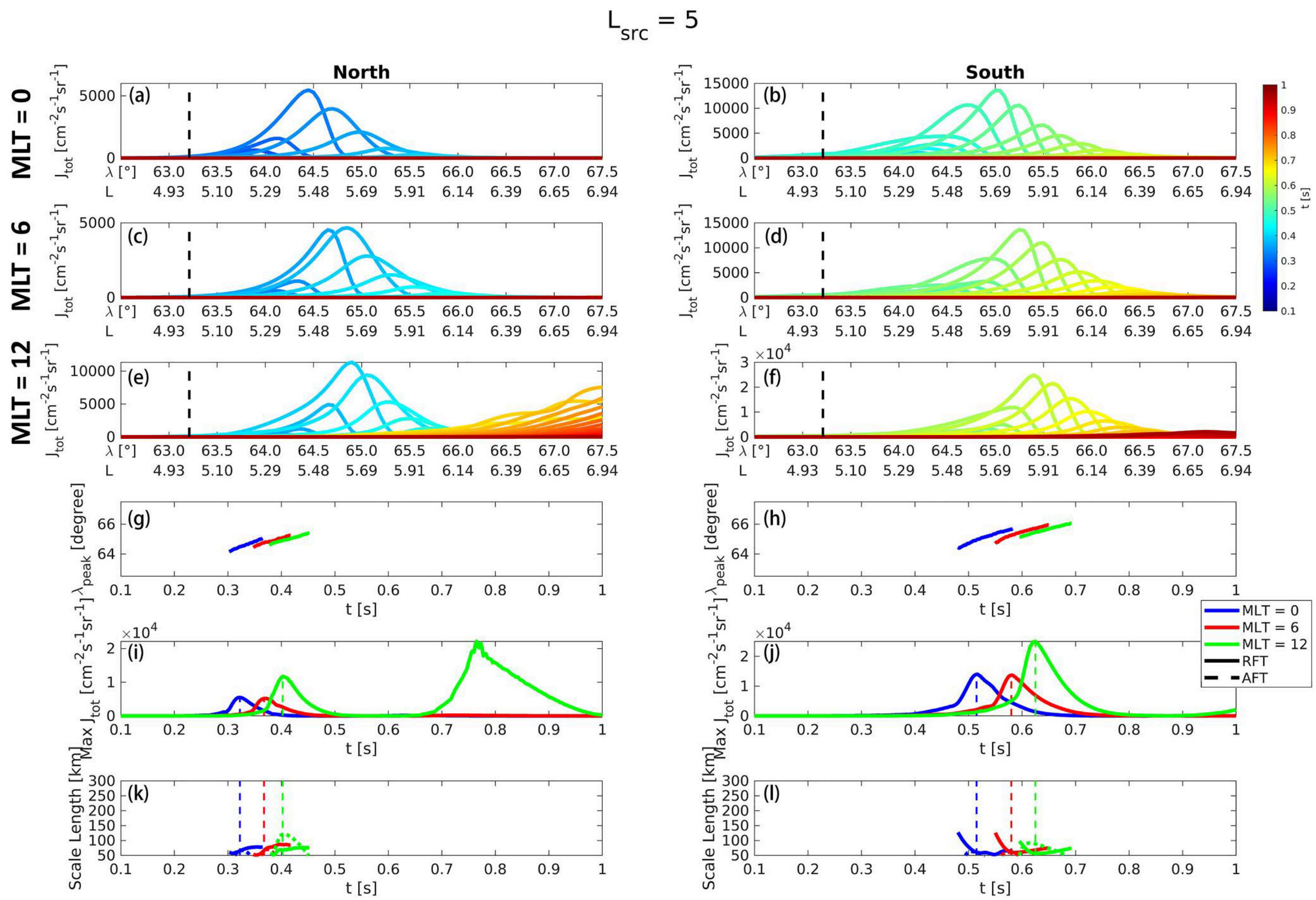

Figure 5. Microburst precipitation flux information for the three runs where chorus wave source region is at Lsrc = 5. (a)–(f) The total relativistic precipitation flux (>1 MeV) spatiotemporal distribution for chorus wave source region at MLT = 0, 6, and 12 (row 1, 2, and 3) and for northern and southern hemispheres (left and right column). The *y*-axes are the total relativistic precipitation flux, and the *x*-axes are the location represented both by the magnetic latitude λ and the L shell of the field line whose invariant latitude is λ. Curves with different colors are the precipitation flux spatial distributions at different times, shown color coded by the color bar at the top right, with the chorus wave element launched from the equatorial source region defined as $t = 0$. The vertical black dashed line in each panel marks the invariant latitude of the chorus wave source region. (g)–(h) The latitude of maximum total relativistic precipitation flux at each time step. (i)–(j) The maximum total relativistic precipitation flux at each time step as a function of time, for northern (i) and southern (j) hemispheres. Different colors are for different MLT, as indicated by the legend. (k)–(l) The scale length at each time step, for northern (k) and southern (l) hemispheres. Different colors are for different MLT, and solid and dashed curves are the scale length under the relative flux threshold and absolute flux threshold definition. Color is the same as in panels (g)–(j).

3.3. Microburst Spatiotemporal Distribution

A precipitation E-t spectrum such as the one shown in Figure 4 provides detailed temporal information about the precipitation along a single field line, or equivalently, temporal precipitation information at only two single points on the ground (which are the two foot points of the field line in each hemisphere). By integrating the precipitation flux of one field line above 1 MeV (the white dashed lines in Figure 4), we can obtain the temporal variation of the total relativistic precipitation flux $J(t;\lambda)$ for one ground location with the corresponding invariant latitude λ. In this work, we calculate the precipitation flux signatures for 300 field lines whose invariant latitudes are evenly spaced between 62.5° and 68.5°, thus constructing a complete spatiotemporal distribution $J(t,\lambda)$ of the relativistic precipitation induced by a single chorus wave element.

The results are shown in panels (a)–(f) of Figures 5–7. Figures 5–7 correspond to chorus wave source region located at $L = 5$, 5.5 and 6, respectively. In each figure, the panels in the left columns are for precipitation occurring in the northern hemisphere, and panels in the right columns are for southern hemisphere; the first three rows are the precipitation spatiotemporal distribution for chorus wave source region at MLT = 0, 6, and 12. The *y*-axes are the total relativistic precipitation flux, and the *x*-axes are the location represented both by the magnetic latitude λ and the L shell of the field line whose invariant latitude is λ. Curves with different colors are the

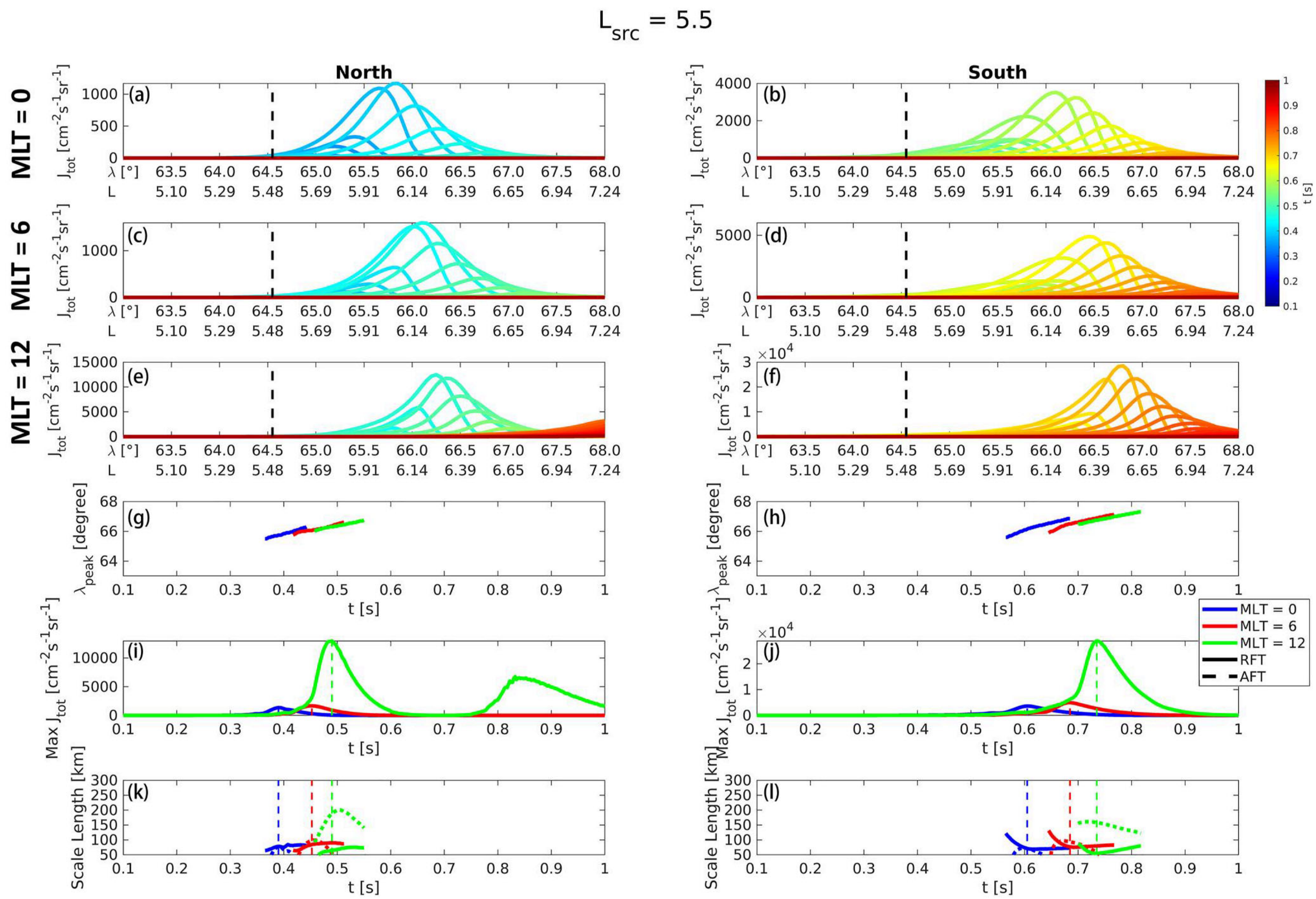

Figure 6. All notations are the same as Figure 5 but Lsrc = 5.5.

precipitation flux spatial distributions at different times, shown color coded by the color bar at the top right, with the chorus wave element launched from the equatorial source region defined as $t = 0$. The vertical black dashed line in each panel marks the invariant latitude of the chorus wave source region.

Several properties can be observed and understood from these precipitation flux spatiotemporal distributions. First, it is seen that the relativistic electron microburst was successfully reproduced in each panel, with the flux profile taking the form of a single peak that grows and decays within ∼0.2 s, consistent with the typical time duration of a microburst (e.g., Imhof et al., 1992; Tsurutani et al., 2013). In all cases, the microburst occurs poleward of the foot point of the chorus wave source region (marked by the vertical black dashed line in each panel), and the microburst peak keeps moving poleward throughout the entire duration of the event. Panels (k) and (l) of Figures 5–7 show the latitude of the maximum precipitated flux as a function of time, and the different colors show different source MLTs as indicated by the legend. We see that in all cases the peak of the microburst keeps moving poleward, and the ground velocity estimated by $R_E \frac{d\lambda}{dt}$ is 700–1,000 km/s. This is a consequence of the chorus wave propagation effect, namely that the chorus wave power propagates to higher L shells, as we discussed in Sections 3.1 and 3.2. The microburst in the southern hemisphere occurs later than those in the northern hemisphere because the chorus waves propagate only northward. As a result, the wave-particle interactions occur in the northern hemisphere, and thus more flight distance is required for electrons to travel from the interaction location to southern hemisphere foot point than northern hemisphere resulting in a longer delay to the onset of the precipitation signature. However, the precipitation flux in the southern hemisphere is stronger than the northern hemisphere because the counter-streaming cyclotron resonance (which results in precipitation occurring in the southern hemisphere) leads to more efficient PA scattering than the co-streaming anomalous cyclotron resonance.

In comparing the microburst properties between different L shells and MLTs, we notice that microbursts occur earlier at lower L shells and MLTs closer to midnight, compared to those at higher L shells and the dayside source

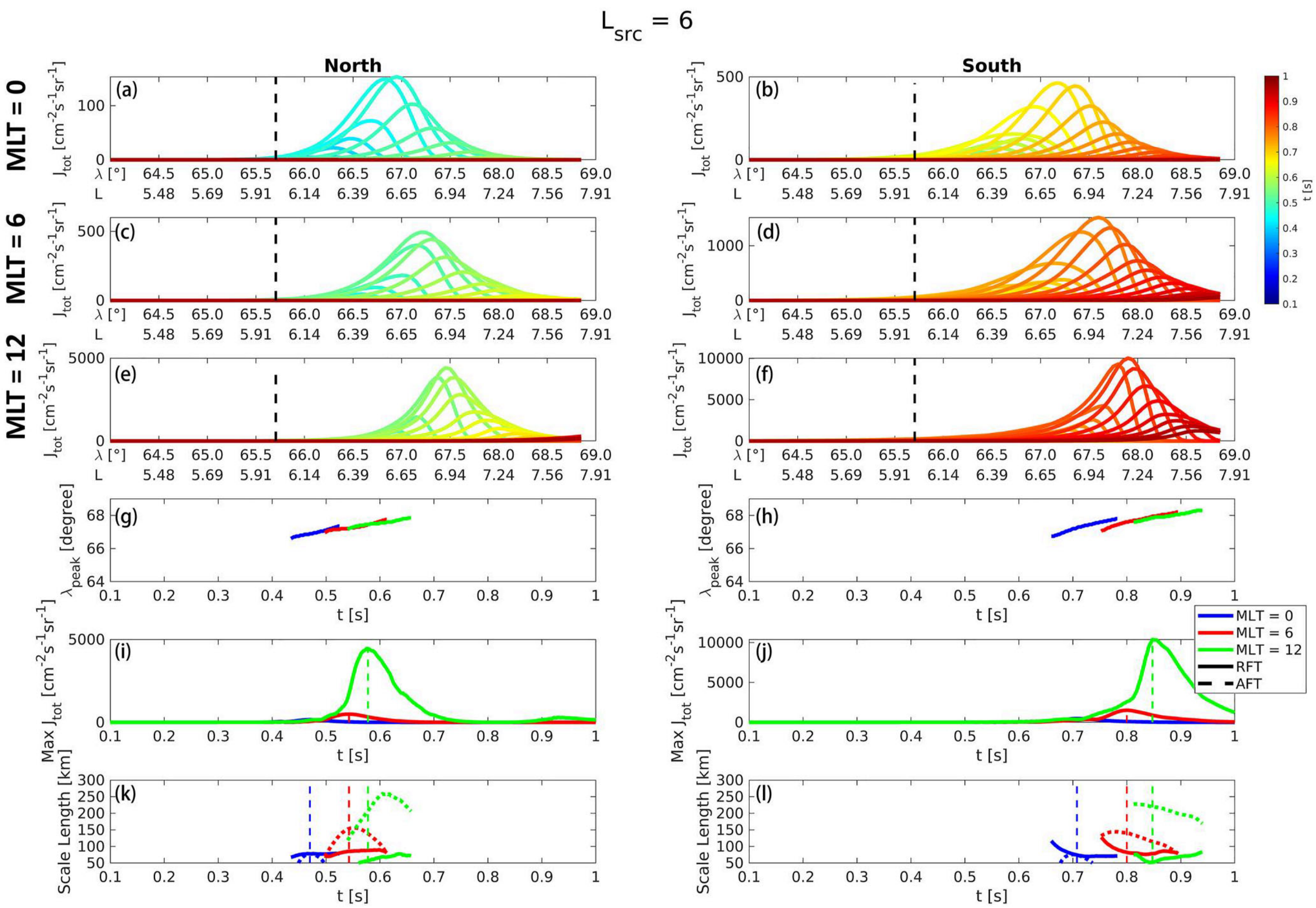

Figure 7. All notations are the same as Figure 5 but Lsrc = 6.

regions. The L shell dependence is due to shorter field line length at lower L shells, which reduces both the time waves propagate from the equatorial source to the wave-particle interaction region and the electron flight time from interaction region to the ground. The MLT dependence is because of the fact that cold electron density increases from the nightside to the dayside (see Figure 1b), which means an increasing refractive index or decreasing phase and group velocities, thus it takes longer for chorus waves to propagate from the equator to the wave-particle interaction location. We also note that in moving from the nightside to the dayside, microbursts occur at progressively higher latitudes. This might be due to a number of factors, including an increasing cold electron density radial gradient from nightside to dayside (see Figure 1b), which leads to a larger radial group velocity according to Snell's Law, as well as decreasing suprathermal fluxes (responsible for Landau damping) which causes longer propagation paths extending to higher latitudes and L-shells.

We also see that the total relativistic precipitation flux is much stronger on the dayside compared to the night and dawn sides. To better illustrate this, we plot the maximum total relativistic precipitation flux $J_m(t)$ in panels (g) and (h) of Figures 5–7. The x-axis is time, and the y-axis is the instantaneous maximum flux $J_m(t) = \max[J(t,\lambda)]_\lambda$. The subscript λ means the maximum value across all λ for a given t. The blue, red and green curves are for MLT = 0, 6, and 12, respectively. We see that for every source region L shell and for both northern and southern hemispheres, the total flux at MLT = 12 is always much larger than those at MLT = 0 and 6. This is a consequence of the low suprathermal electron fluxes between 1 and 100 keV on the dayside (see Figure 1b), and indeed both Figures 3g–3i and 4a part (ii), show that the typical Landau resonance energy range is 1–100 keV. Dayside electron flux in this energy range being 1–2 orders of magnitudes lower than MLT = 0 and 6 means a much lower Landau damping rates on the dayside, which makes it possible for chorus waves to maintain high wave power at high latitudes on dayside, as can be seen from Figures 2c, 2f, and 2i. It is this much larger wave power on the dayside that makes the electron scattering much more efficient at ∼MeV energies, thus leads to a much larger relativistic electron microburst precipitation flux.

3.4. Microburst Scale Size

Using the precipitation flux spatial distributions at each time, such as those in panels (a)–(f) of Figures 5–7, we can analyze the spatial characteristics of the microburst such as the scale size. To define the scale size of microburst at a given time, we need a flux threshold $J_{th}(t)$, roughly corresponding to the fact that a satellite-based particle detector could measure a precipitation signature above some given noise floor or minimum counting rate. Because the flux spatial profile is always a simple single-peak structure, we can find the lowest and highest latitudes λ_{min} and λ_{max} at each time step between which the flux exceeds the threshold level $J(t,\lambda) \geq J_{th}(t)$, $\lambda_{min} < \lambda < \lambda_{max}$. Thereafter, we can define the scale size at each time step as $d(t) = (\lambda_{max} - \lambda_{min})R_E$.

We use two different definitions for the flux threshold $J_{th}(t)$. Following the method of Shumko et al. (2021), we define $J_{th}(t) = \frac{1}{2}J_m(t)$. In this way, J_{th} varies with time as the maximum flux changes, and the scale size is actually defined as the full width at half maximum (FWHM) of the flux spatial distribution, and is not an absolute threshold. We call this definition the relative flux threshold (RFT). We also use a fixed-value version of J_{th}, which is given by $J_{th} = \frac{1}{2}\max[J_m(t,\text{MLT} = 0)]_t$, corresponding to half of the maximum instantaneous maximum flux at MLT = 0 which is more consistent with a satellite-based detector observation above some given noise floor or minimum counting rate. For all the cases with chorus wave source region at the same L shell, we use this flux threshold to define the scale size. We call this definition the absolute flux threshold (AFT). The reason for using this alternative definition is that the dayside precipitated flux is much larger than dawn and night sides, which leads to a potentially misleading comparison if only FWHM is considered. Under the RFT definition, the dayside will use a much larger J_{th} than dawn and night sides, so the results may appear distorted. Using both definitions gives a more complete picture. The AFT definition is also provided to facilitate the comparison against various microburst selection methods in observational studies, which may be based on either the absolute fluctuation of the precipitation flux or the relative formulation.

We now present the scale length results in panels (i) and (j) of Figures 5–7, where panels (i) correspond to the northern hemisphere and panels (j) to the southern hemisphere. Different colors represent different MLTs, similar to panels (g) and (h). The solid and dashed curves are the scale lengths for the RFT and AFT definitions, respectively. We can see that the RFT scale lengths are usually between 50 and 100 km, which agrees well with previous observational studies (Blake et al., 1996; Crew et al., 2016; Parks, 1967; Shumko et al., 2018, 2020). On the other hand, the AFT scale lengths are also between 50 and 100 km for MLT = 0 and 6, but can be as large as 150 ∼ 300 km for MLT = 12. This is a direct consequence of the significantly stronger precipitation flux on the dayside compared to the night and dawn sides.

To further compare the global distribution characteristics of the scale length, we choose one representative scale length for each case, which is chosen to be the scale length when $J_m(t)$ reaches its maximum, as indicated by the vertical dashed lines in panels (g)–(j) of Figures 5–7. The scale lengths corresponding to the intersection point between the vertical dashed line and the curves in panels (i) and (j) are the representative scale lengths. The global distributions of the scale length and the maximum total relativistic precipitation flux are shown in Figure 8, where we use MLT = 0, 6, and 12 to represent the whole midnight, dawn and noon sectors for a better illustration of a general global trend.

From Figure 8 we can clearly see that the noon sector has distinct characteristics than the dawn and midnight sectors. The dawn and midnight sectors have little differences in terms of maximum fluxes and scale sizes and share the same trends that the precipitation flux is stronger in the inner L shells and the scale size is larger in the outer L shells. However, for the noon sector, the maximum flux is about one order of magnitude stronger than the dawn and midnight sectors, and the scale size is significantly smaller using RFT and larger using AFT, compared with the other two sectors. The RFT scale sizes in the noon sector also show an opposite trend as the other two sectors that the scale size is smaller in the outer L shells.

4. Discussion and Summary

A few features became apparent from the detailed spatiotemporal signatures of the precipitation flux (Figures 5–7) as well as the resultant scale sizes presented in Figure 8. The first feature is that the scale size of the relativistic

10.1029/2023JA032250

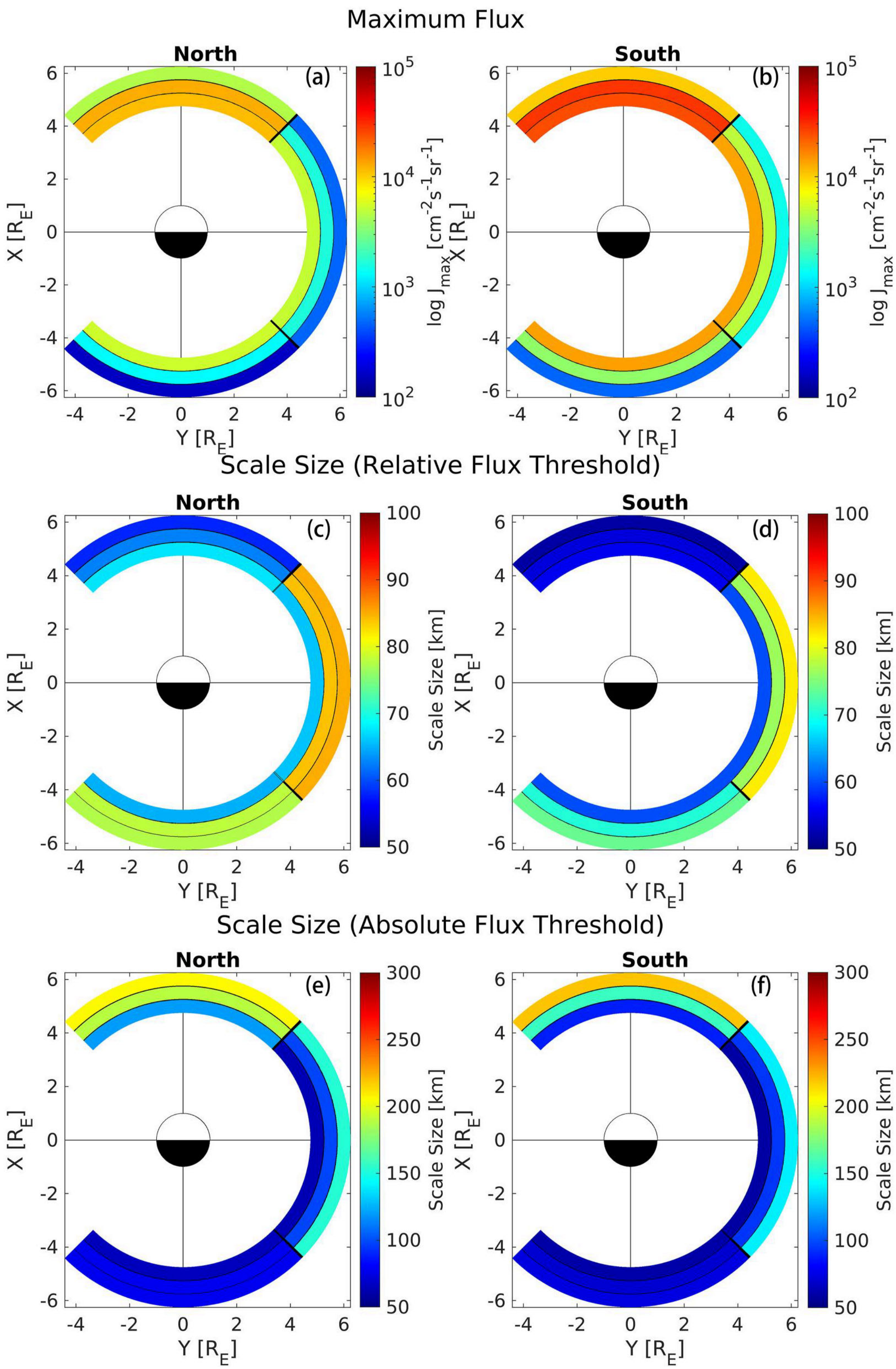

Figure 8. (a)–(b) The maximum total precipitation flux over all latitude and time steps in each run. The centers of bins in each panel represent the locations of the chorus wave source point. Color coded is the maximum total precipitation flux as indicated by the color bar. The format is the same for panels (c)–(f). (c)–(d) are the scale size under relative flux threshold definition, and (e)–(f) are the scale size under absolute flux threshold definition. Panels on the left/right column are for northern/southern hemisphere.

microbursts in the noon sector was seen to be smaller than that at the dawn and midnight sectors under the RFT definition. This smaller scale size is due to the weak Landau damping on the dayside, which we have shown to be a dominant controller of many characteristics of the precipitation flux. A related feature is the fact that the range of L shells covered by the chorus wave paths appeared to shrink as latitude increases, as a result of the chorus ray paths on the Earthward side propagating further outward and getting damped quicker, resulting in an overall convergence effect of the rays. Therefore, if most of the wave-particle interaction happens at lower latitudes, the precipitated area mapped to the ground will be larger, resulting in a larger scale size. However, Figure 3 shows that the >1 MeV resonance energies are typically only found at latitudes above 25°, and Figure 2 shows that the wave powers in MLT = 0 or 6 are mostly confined below 30°, which means for midnight and dawn sectors, the scattering of relativistic electrons occurs at the widest L-shell-coverage area at the lowest possible latitudes for relativistic electron scattering. In contrast, waves in the noon sector are weakly damped and can maintain a considerable power at higher latitude for strong relativistic electron scattering, at which region the waves cover a narrower range of L shells. Therefore, we would expect the scale size of the relativistic microburst in MLT = 12 to be smaller.

One chorus wave feature that is not included in the present work is the chirping of the chorus wave element which would tend to increase the duration of the precipitation signature to some extent. In the ray tracing modeling, all rays with different frequencies are launched simultaneously, thus in effect assuming an infinitely large chirping rate in order to focus only on the wave propagation and electron time-of-flight aspects. Test runs show that finite chirping rates do have some impacts on the spatial precipitation flux distribution (Chen et al., 2020, 2021; Miyoshi et al., 2010; Saito et al., 2012) but that it is a less important factor compared with other factors, especially the effects of MLT. This might be due to the fact that the scale size is a spatial characteristic and will be less affected by the temporal characteristics like the chirping rate. Therefore, we neglect the wave frequency chirping in this work to focus solely on propagation effects, eliminate one variable from consideration to reduce the complexity of the analysis, and leave the chirping rate effects for future detailed study.

Both our present study and Shumko et al. (2021) indicate that the dayside is very special in terms of the spatiotemporal characteristics of relativistic electron microbursts. However, there is potential to misinterpret the results of these two works since Shumko et al. (2021) finds that the duration of relativistic microbursts is larger on the dayside while our work suggests that the scale size is smaller, if we follow the same FWHM definition, which may lead to the incorrect conclusion that our modeling results are in conflict with existing observational results. It is important to note that we analyze purely the spatial characteristics in this work, while in the work of Shumko et al. (2021), their method of directly analyzing the in situ time history of precipitation flux implies that they analyze almost purely temporal characteristics. To support this statement, we estimate the distance traveled by the LEO satellite during one microburst by multiplying the orbital speed (∼7.9 km/s for LEO) and a typical microburst time duration (∼0.2 s), which gives only ∼1.6 km, a value that is one or two orders of magnitude smaller than the typical scale size of the microburst (10–100s km, from Figure 8). Therefore, the spacecraft can be assumed to be essentially stationary during the entire microburst measurement, so the time duration calculated by Shumko et al. (2021) is a purely temporal signature observed from a fixed location, and cannot be directly compared with our purely spatial signature. However, both works indicate the uniqueness of dayside for relativistic microburst, although one from the time perspective (Shumko et al., 2021) and one from the space perspective (this work). The more detailed and complex temporal dimension modeling and comparison with observation is ongoing in future works.

In summary, following the method for modeling the chorus-induced precipitation flux spatial characteristics developed by Kang et al. (2022), we extended the modeling work to several chorus wave source locations distributed over L shells and MLTs, thus trying to model the global distribution of the relativistic microburst spatial characteristics. The model setup is based on statistical results of chorus wave characteristics and electron populations. The relativistic microburst was successfully reproduced for all runs. We comprehensively analyzed the connection between the wave propagation and the precipitation properties. The contribution from different resonance modes to the E-t spectrum of the precipitation flux was identified, and we found that the relativistic microburst was induced through a combination of normal and anomalous cyclotron resonances during counter-stream and co-streaming in the two hemispheres, and the wave-particle interaction region was located at high latitudes (>20°) and a higher L shell compared to the chorus source region, which was assumed to be at equator. We also found that the relativistic microburst occurs poleward of the chorus wave source region, and it continues moving poleward at a ground velocity of 700–1,000 km/s. These features are also related to the chorus wave propagation properties where most of the ray power propagates to larger L shells. The maximum precipitation flux and the scale size of the relativistic microburst are defined and compared among different L shells and MLTs. We found that the characteristics of microburst in the dawn and midnight sectors have little difference, but microbursts in the noon sector have much larger precipitation fluxes, much smaller RFT scale sizes and much larger AFT scale sizes. This is attributed to the much weaker 1–100 keV trapped electron fluxes in the dayside, which lead to a much weaker Landau damping and resultant wave propagation to higher latitudes which have access to resonate with MeV electrons. Thus, our results indicate a controlling effect of keV electron populations on the MeV electron precipitation. This work serves as a theoretical reference for future observational and statistical studies dealing with the relativistic electron microburst scale size, and is also an important step to a global modeling of quantifying the total contribution of chorus wave induced relativistic microburst.

Data Availability Statement

The modeling data from this study are available at the public data via https://doi.org/10.5281/zenodo.10064788.

Acknowledgments
The authors thank the Van Allen Probes teams. This work is supported by NASA FINESST award 80NSSC21K1393 and NSF Geospace Environment Modeling Grant AGS-2025706. QM would like to acknowledge the NASA Grant 80NSSC20K0196 and NSF grant AGS-2225445.

References

Agapitov, O., Mourenas, D., Artemyev, A., Mozer, F. S., Bonnell, J. W., Angelopoulos, V., et al. (2018). Spatial extent and temporal correlation of chorus and hiss: Statistical results from multipoint THEMIS observations. *Journal of Geophysical Research: Space Physics*, *123*(10), 8317–8330. https://doi.org/10.1029/2018ja025725

Anderson, K. A., & Milton, D. W. (1964). Balloon observations of X rays in the auroral zone: 3. High time resolution studies. *Journal of Geophysical Research*, *69*(21), 4457–4479. https://doi.org/10.1029/jz069i021p04457

Blake, J. B., Looper, M. D., Baker, D. N., Nakamura, R., Klecker, B., & Hovestadt, D. (1996). New high temporal and spatial resolution measurements by SAMPEX of the precipitation of relativistic electrons. *Advances in Space Research*, *18*(8), 171–186. https://doi.org/10.1016/0273-1177(95)00969-8

Bortnik, J., Chen, L., Li, W., Thorne, R. M., & Horne, R. B. (2011). Modeling the evolution of chorus waves into plasmaspheric hiss. *Journal of Geophysical Research*, *116*(A8). https://doi.org/10.1029/2011ja016499

Bortnik, J., Inan, U. S., & Bell, T. F. (2003). Frequency-time spectra of magnetospherically reflecting whistlers in the plasmasphere. *Journal of Geophysical Research*, *108*(A1). https://doi.org/10.1029/2002ja009387

Bortnik, J., Inan, U. S., & Bell, T. F. (2006a). Temporal signatures of radiation belt electron precipitation induced by lightning-generated MR whistler waves: 1. Methodology. *Journal of Geophysical Research*, *111*(A2). https://doi.org/10.1029/2005ja011182

Bortnik, J., Inan, U. S., & Bell, T. F. (2006b). Temporal signatures of radiation belt electron precipitation induced by lightning-generated MR whistler waves: 2. Global signatures. *Journal of Geophysical Research*, *111*(A2). https://doi.org/10.1029/2005ja011398

Bortnik, J., & Thorne, R. M. (2007). The dual role of ELF/VLF chorus waves in the acceleration and precipitation of radiation belt electrons. *Journal of Atmospheric and Solar-Terrestrial Physics*, *69*(3), 378–386. https://doi.org/10.1016/j.jastp.2006.05.030

Bortnik, J., Thorne, R. M., & Meredith, N. P. (2007). Modeling the propagation characteristics of chorus using CRRES suprathermal electron fluxes. *Journal of Geophysical Research*, *112*(A8). https://doi.org/10.1029/2006ja012237

Breneman, A. W., Crew, A., Sample, J., Klumpar, D., Johnson, A., Agapitov, O., et al. (2017). Observations directly linking relativistic electron microbursts to whistler mode chorus: Van Allen Probes and FIREBIRD II. *Geophysical Research Letters*, *44*(22), 11–265. https://doi.org/10.1002/2017gl075001

Brinca, A. L. (1972). On the stability of obliquely propagating whistlers. *Journal of Geophysical Research*, *77*(19), 3495–3507. https://doi.org/10.1029/ja077i019p03495

Carpenter, D. L., & Anderson, R. R. (1992). An ISEE/whistler model of equatorial electron density in the magnetosphere. *Journal of Geophysical Research*, *97*(A2), 1097–1108. https://doi.org/10.1029/91ja01548

Chen, L., Breneman, A. W., Xia, Z., & Zhang, X. J. (2020). Modeling of bouncing electron microbursts induced by ducted chorus waves. *Geophysical Research Letters*, *47*(17), e2020GL089400. https://doi.org/10.1029/2020gl089400

Chen, L., Zhang, X. J., Artemyev, A., Zheng, L., Xia, Z., Breneman, A. W., & Horne, R. B. (2021). Electron microbursts induced by nonducted chorus waves. *Frontiers in Astronomy and Space Sciences*, *8*, 745927. https://doi.org/10.3389/fspas.2021.745927

Crew, A. B., Spence, H. E., Blake, J. B., Klumpar, D. M., Larsen, B. A., O'Brien, T. P., et al. (2016). First multipoint in situ observations of electron microbursts: Initial results from the NSF FIREBIRD II mission. *Journal of Geophysical Research: Space Physics*, *121*(6), 5272–5283. https://doi.org/10.1002/2016ja022485

Douma, E., Rodger, C. J., Blum, L. W., & Clilverd, M. A. (2017). Occurrence characteristics of relativistic electron microbursts from SAMPEX observations. *Journal of Geophysical Research: Space Physics*, *122*(8), 8096–8107. https://doi.org/10.1002/2017ja024067

Douma, E., Rodger, C. J., Blum, L. W., O'Brien, T. P., Clilverd, M. A., & Blake, J. B. (2019). Characteristics of relativistic microburst intensity from SAMPEX observations. *Journal of Geophysical Research: Space Physics*, *124*(7), 5627–5640. https://doi.org/10.1029/2019ja026757

Hikishima, M., Omura, Y., & Summers, D. (2010). Microburst precipitation of energetic electrons associated with chorus wave generation. *Geophysical Research Letters*, *37*(7). https://doi.org/10.1029/2010gl042678

Horne, R. B., & Thorne, R. M. (2003). Relativistic electron acceleration and precipitation during resonant interactions with whistler-mode chorus. *Geophysical Research Letters*, *30*(10). https://doi.org/10.1029/2003gl016973

Imhof, W. L., Voss, H. D., Mobilia, J., Datlowe, D. W., Gaines, E. E., McGlennon, J. P., & Inan, U. S. (1992). Relativistic electron microbursts. *Journal of Geophysical Research*, *97*(A9), 13829–13837. https://doi.org/10.1029/92ja01138

Inan, U. S., & Bell, T. F. (1977). The plasmapause as a VLF wave guide. *Journal of Geophysical Research*, *82*(19), 2819–2827. https://doi.org/10.1029/ja082i019p02819

Kang, N. (2023). Modelling the global distribution of chorus wave induced relativistic microburst spatial scale size [Dataset]. *Zenodo*. https://doi.org/10.5281/zenodo.10064788

Kang, N., & Bortnik, J. (2022). Structure of energy precipitation induced by superbolt-lightning generated whistler waves. *Geophysical Research Letters*, *49*(5), e2022GL097770. https://doi.org/10.1029/2022gl097770

Kang, N., Bortnik, J., Zhang, X., Claudepierre, S., & Shi, X. (2022). Relativistic microburst scale size induced by a single point-source chorus element. *Geophysical Research Letters*, *49*(23), e2022GL100841. https://doi.org/10.1029/2022gl100841

Kersten, K., Cattell, C. A., Breneman, A., Goetz, K., Kellogg, P. J., Wygant, J. R., et al. (2011). Observation of relativistic electron microbursts in conjunction with intense radiation belt whistler-mode waves. *Geophysical Research Letters*, *38*(8). https://doi.org/10.1029/2011gl046810

Kimura, I. (1966). Effects of ions on whistler-mode ray tracing. *Radio Science*, *1*(3), 269–283. https://doi.org/10.1002/rds196613269

Li, W., Thorne, R. M., Angelopoulos, V., Bortnik, J., Cully, C. M., Ni, B., et al. (2009). Global distribution of whistler-mode chorus waves observed on the THEMIS spacecraft. *Geophysical Research Letters*, *36*(9). https://doi.org/10.1029/2009gl037595

Lorentzen, K. R., Blake, J. B., Inan, U. S., & Bortnik, J. (2001). Observations of relativistic electron microbursts in association with VLF chorus. *Journal of Geophysical Research*, *106*(A4), 6017–6027. https://doi.org/10.1029/2000ja003018

Lorentzen, K. R., Looper, M. D., & Blake, J. B. (2001). Relativistic electron microbursts during the GEM storms. *Geophysical Research Letters*, *28*(13), 2573–2576. https://doi.org/10.1029/2001gl012926

Ma, Q., Connor, H. K., Zhang, X. J., Li, W., Shen, X. C., Gillespie, D., et al. (2020). Global survey of plasma sheet electron precipitation due to whistler mode chorus waves in Earth's magnetosphere. *Geophysical Research Letters*, *47*(15), e2020GL088798. https://doi.org/10.1029/2020gl088798

Miyoshi, Y., Katoh, Y., Nishiyama, T., Sakanoi, T., Asamura, K., & Hirahara, M. (2010). Time of flight analysis of pulsating aurora electrons, considering wave-particle interactions with propagating whistler mode waves. *Journal of Geophysical Research*, *115*(A10). https://doi.org/10.1029/2009ja015127

Miyoshi, Y., Oyama, S., Saito, S., Kurita, S., Fujiwara, H., Kataoka, R., et al. (2015). Energetic electron precipitation associated with pulsating aurora: EISCAT and Van Allen Probe observations. *Journal of Geophysical Research: Space Physics*, *120*(4), 2754–2766. https://doi.org/10.1002/2014ja020690

Miyoshi, Y., Saito, S., Kurita, S., Asamura, K., Hosokawa, K., Sakanoi, T., et al. (2020). Relativistic electron microbursts as high-energy tail of pulsating aurora electrons. *Geophysical Research Letters*, *47*(21), e2020GL090360. https://doi.org/10.1029/2020gl090360

Nakamura, R., Isowa, M., Kamide, Y., Baker, D. N., Blake, J. B., & Looper, M. (2000). SAMPEX observations of precipitation bursts in the outer radiation belt. *Journal of Geophysical Research*, *105*(A7), 15875–15885. https://doi.org/10.1029/2000ja900018

Nishimura, Y., Bortnik, J., Li, W., Thorne, R. M., Chen, L., Lyons, L. R., et al. (2011). Multievent study of the correlation between pulsating aurora and whistler mode chorus emissions. *Journal of Geophysical Research*, *116*(A11). https://doi.org/10.1029/2011ja016876

Nishimura, Y., Bortnik, J., Li, W., Thorne, R. M., Lyons, L. R., Angelopoulos, V., et al. (2010). Identifying the driver of pulsating aurora. *Science*, *330*(6000), 81–84. https://doi.org/10.1126/science.1193186

O'brien, T. P., Lorentzen, K. R., Mann, I. R., Meredith, N. P., Blake, J. B., Fennell, J. F., et al. (2003). Energization of relativistic electrons in the presence of ULF power and MeV microbursts: Evidence for dual ULF and VLF acceleration. *Journal of Geophysical Research*, *108*(A8). https://doi.org/10.1029/2002ja009784

Ozaki, M., Inoue, T., Tanaka, Y., Yagitani, S., Kasahara, Y., Shiokawa, K., et al. (2021). Spatial evolution of wave-particle interaction region deduced from flash-type auroras and chorus-ray tracing. *Journal of Geophysical Research: Space Physics*, *126*(7), e2021JA029254. https://doi.org/10.1029/2021ja029254

Ozaki, M., Yagitani, S., Shiokawa, K., Tanaka, Y., Ogawa, Y., Hosokawa, K., et al. (2022). Slow contraction of flash aurora induced by an isolated chorus element ranging from lower-band to upper-band frequencies in the source region. *Geophysical Research Letters*, *49*(9), e2021GL097597. https://doi.org/10.1029/2021gl097597

Pailoor, N., Cohen, M., Richardson, D., Harid, V., & Gołkowski, M. (2023). Quantification of lightning-induced electron precipitation events on electron fluxes in the radiation belts. *Journal of Geophysical Research: Space Physics*, *128*(9), e2022JA031153. https://doi.org/10.1029/2022ja031153

Parks, G. K. (1967). Spatial characteristics of auroral-zone X-ray microbursts. *Journal of Geophysical Research*, *72*(1), 215–226. https://doi.org/10.1029/jz072i001p00215

Saito, S., Miyoshi, Y., & Seki, K. (2012). Relativistic electron microbursts associated with whistler chorus rising tone elements: GEMSIS-RBW simulations. *Journal of Geophysical Research*, *117*(A10). https://doi.org/10.1029/2012ja018020

Shumko, M., Blum, L. W., & Crew, A. B. (2021). Duration of individual relativistic electron microbursts: A probe into their scattering mechanism. *Geophysical Research Letters*, *48*(17), e2021GL093879. https://doi.org/10.1029/2021gl093879

Shumko, M., Johnson, A. T., Sample, J. G., Griffith, B. A., Turner, D. L., O'Brien, T. P., et al. (2020). Electron microburst size distribution derived with AeroCube-6. *Journal of Geophysical Research: Space Physics*, *125*(3), e2019JA027651. https://doi.org/10.1029/2019ja027651

Shumko, M., Sample, J., Johnson, A., Blake, B., Crew, A., Spence, H., et al. (2018). Microburst scale size derived from multiple bounces of a microburst simultaneously observed with the FIREBIRD-II CubeSats. *Geophysical Research Letters*, *45*(17), 8811–8818. https://doi.org/10.1029/2018gl078925

Smith, R. L., & Angerami, J. J. (1968). Magnetospheric properties deduced from OGO 1 observations of ducted and nonducted whistlers. *Journal of Geophysical Research*, *73*(1), 1–20. https://doi.org/10.1029/ja073i001p00001

Thorne, R. M., Ni, B., Tao, X., Horne, R. B., & Meredith, N. P. (2010). Scattering by chorus waves as the dominant cause of diffuse auroral precipitation. *Nature*, *467*(7318), 943–946. https://doi.org/10.1038/nature09467

Thorne, R. M., O'Brien, T. P., Shprits, Y. Y., Summers, D., & Horne, R. B. (2005). Timescale for MeV electron microburst loss during geomagnetic storms. *Journal of Geophysical Research*, *110*(A9). https://doi.org/10.1029/2004ja010882

Tsurutani, B. T., Lakhina, G. S., & Verkhoglyadova, O. P. (2013). Energetic electron (>10 keV) microburst precipitation, ~5–15s X-ray pulsations, chorus, and wave-particle interactions: A review. *Journal of Geophysical Research: Space Physics*, *118*(5), 2296–2312. https://doi.org/10.1002/jgra.50264

Zhang, X. J., Angelopoulos, V., Mourenas, D., Artemyev, A., Tsai, E., & Wilkins, C. (2022). Characteristics of electron microburst precipitation based on high-resolution ELFIN measurements. *Journal of Geophysical Research: Space Physics*, *127*(5), e2022JA030509. https://doi.org/10.1029/2022ja030509